An advanced synthetic eddy method for the computation of aerofoil-turbulence interaction noise

Jae Wook Kim, Sina Haeri

Aerodynamics & Flight Mechanics Research Group, University of Southampton, Southampton, SO17 1BJ, United Kingdom

Abstract

This paper presents an advanced method to synthetically generate flow turbulence via an inflow boundary condition particularly designed for three-dimensional aeroacoustic simulations. The proposed method is virtually free of spurious noise that might arise from the synthetic turbulence, which enables a direct calculation of propagated sound waves from the source mechanism. The present work stemmed from one of the latest outcomes of synthetic eddy method (SEM) derived from a well-defined vector potential function creating a divergence-free velocity field with correct convection speeds of eddies, which in theory suppresses pressure fluctuations. In this paper, a substantial extension of the SEM is introduced and systematically optimised to create a realistic turbulence field based on von Kármán velocity spectra. The optimized SEM is then combined with a well-established sponge-layer technique to quietly inject the turbulent eddies into the domain from the upstream boundary, which results in a sufficiently clean acoustic field. Major advantages in the present approach are: a) that genuinely three-dimensional turbulence is generated; b) that various ways of parametrisation can be created to control/characterise the randomly distributed eddies; and, c) that its numerical implementation is efficient as the size of domain section through which the turbulent eddies should be passing can be adjusted and minimised. The performance and reliability of the proposed SEM are demonstrated by a three-dimensional simulation of aerofoil-turbulence interaction noise.

Keywords: , Synthetic eddy method (SEM); Inflow turbulence; Computational aeroacoustics (CAA); Aerofoil-turbulence interaction (ATI)

Email address: j.w.kim@soton.ac.uk (Jae Wook Kim)

1. Introduction

The generation of synthetic turbulent flows is currently one of the challenging issues in computational aeroacoustics (CAA). It has a significant impact on the simulation of important engineering problems such as aerofoil-turbulence interaction noise that is related to turbofan engines, open rotors, wind turbines, helicopters, etc. There are a few crucial properties that a synthetic turbulence has to satisfy/offer in order to achieve a successful CAA simulation: 1) divergence-free condition, 2) synchronised convection with the mean flow, 3) statistical characteristics of realistic turbulence and 4) genuinely three-dimensional capabilities. Failure to meet all these criteria would result in either spurious noise that contaminates the far-field acoustic data or incorrect source mechanisms at the near field. In addition, the generation of synthetic turbulence should be numerically efficient not to overload the entire simulation.

Over the past years, various techniques of generating synthetic turbulence have been proposed and they mostly stemmed from incompressible flows background. Some of them have also been applied to compressible/aeroacoustic calculations, which can be categorised into: a) Fourier modes [1–6], b) random particle meshes [7, 8] and c) synthetic eddy method (SEM) [9–12]. The Fourier-mode based approach is probably one of the most frequently attempted methods for CAA applications due to its simplicity to generate a divergence-free velocity field by taking the cross product of the wavenumber and amplitude vectors. The divergence-free condition is crucial for CAA applications to prevent spurious artefact noise that may emerge from the synthetically generated turbulence. However, this is not the only criterion to achieve noise-free turbulence. Sescu and Hixon [12] found that the convection velocity of the synthetically generated turbulence must be synchronized with the local mean-flow velocity in order to guarantee a clean aeroacoustic environment not interfering with genuine sound waves. Currently the synchronized convection has not been considered in the Fourier-mode approaches. In the meantime, the random-particle-mesh approach has demonstrated some promising results for aeroacoustic simulations but a full three-dimensional (3D) extension is yet to be achieved in the near future.

The synthetic eddy method (SEM) originally proposed by Jarrin *et al.* [9] has recently been extended by Sescu and Hixon [12] for aeroacoustic sim-

ulations. The recent achievement was made by introducing an eddy shape function (vector potential) and taking the curl of the vector potential to create a divergence-free velocity field, where the argument function of the vector potential was properly determined to satisfy the synchronized convection condition highlighted above. Sescu and Hixon [12] showcased through benchmark tests that the new SEM could potentially be the first successful 3D method for noise-free synthetic turbulence aimed at CAA simulations. There still is a significant scope of work to be done to construct "realistic" turbulence statistics based on the new method and demonstrate its actual performance in a large-scale 3D CAA simulation, which is the main focus of this paper.

In this paper, the latest SEM is combined with a sponge-layer technique [13–15] that was particularly designed for introducing velocity disturbances as well as absorbing spurious noise. With this combination, the level of spurious noise is kept sufficiently low to guarantee a clean sound field for CAA simulations. Secondly, new parameters to characterise the randomly distributed eddies (i.e. sizes, locations, directional strengths and the population per volume) are introduced and effectively optimized by using Genetic Algorithm to get the resulting turbulence statistics matched with von Kármán spectra. It should be noted that the optimisation of the eddy parameters is implemented with inclusion of a periodic boundary condition across the lateral boundaries of the domain. The current periodic boundary condition provides C^{∞}-continuity which yields entirely smooth connection of the two lateral boundaries. Thirdly, the stream of the synthetic eddies is confined within a narrow channel passing through the near-field area only rather than the entire domain. This has a significant impact on the numerical efficiency since otherwise very fine meshes must be maintained throughout the entire domain in order to resolve the smallest eddies that are normally much smaller than the corresponding acoustic wavelengths. Lastly, the optimized SEM is applied to a 3D simulation of aerofoil-turbulence interaction noise and the results are compared with existing theoretical prediction and experimental data.

The organisation of this paper is as follows. Section 2 introduces the theoretical background of SEM. Section 3 explains the parametric optimisation of the eddies in order to obtain realistic 3D von Kármán velocity spectra. Section 4 describes the governing equations and the sponge-layer technique used in this paper for quietly injecting the synthetic turbulence into the computational domain. In Sec. 5, a numerical test of the present synthetic turbulence

is carried out in order to verify its low-noise capability and actual turbulence statistics. Section 6 demonstrates the application of the optimised SEM to a 3D simulation of aerofoil-turbulence interaction noise where the performance and reliability of the proposed approach is addressed. Finally, concluding remarks are given in Sec. 7.

2. Synthetic Eddy Model

The present synthetic eddy method (SEM) is based on a vector potential $\mathbf{\Psi}(\mathbf{x}, t)$ proposed by Sescu and Hixon [12], which is constructed by superimposing contributions from randomly distributed vortical eddies. The resulting velocity field induced by the vortical eddies is obtained by taking the curl of the vector potential, i.e. $\mathbf{u}'(\mathbf{x}, t) = \nabla \times \mathbf{\Psi}(\mathbf{x}, t)$, which is divergence free. It is suggested in this paper that an artificial turbulence field with realistic velocity spectra can be constructed by imposing certain regularisations and constraints on the sizes, shapes and directional strengths of the randomly distributed eddies in a 3D space. A general form of the vector potential may be written as:

$$\mathbf{\Psi}(\mathbf{x}, t) = a_\infty \left(\frac{A_\mathrm{e} L_\mathrm{e}}{N_\mathrm{e}} \right)^{\frac{1}{3}} \sum_{i=1}^{N_\mathrm{e}} [\psi_{x,i}(\mathbf{x}, t)\mathbf{e}_x + \psi_{y,i}(\mathbf{x}, t)\mathbf{e}_y + \psi_{z,i}(\mathbf{x}, t)\mathbf{e}_z] \qquad (1)$$

where a_∞ is the ambient speed of sound, L_e is the length of a "virtual" eddy box in which the eddies are created, A_e is the eddy box's cross-section area through which the eddies are injected into the computational domain (hence $A_\mathrm{e} L_\mathrm{e}$ is the volume of the virtual eddy box), N_e is the number of eddies. $(A_\mathrm{e} L_\mathrm{e}/N_\mathrm{e})^{1/3}$ indicates an average distance between two adjacent eddies inside the virtual eddy box. ψ_x, ψ_y and ψ_z are a set of dimensionless shape functions for each individual eddy component. $\mathbf{e}_x$, $\mathbf{e}_y$ and $\mathbf{e}_z$ are the directional unit vectors in the Cartesian coordinate system.

In this paper, Gaussian and Mexican Hat profiles are considered for the shape functions of the eddies. The authors found that the Mexican Hat profile is useful to enhance high-frequency components in the resulting velocity spectra whereas the Gaussian one is more responsible for the low-frequency

components. The present shape functions are defined as:

$$\psi_{\xi,i}(r_i) = \begin{cases} \epsilon_{\xi,i}\, \sigma_{\xi,i}^{-1/2} \exp[-(3\sigma_{\xi,i} r_i)^2] & \text{(Gaussian)} \\ \epsilon_{\xi,i}\, \sigma_{\xi,i}^{-1/2} [1-(4\sigma_{\xi,i} r_i)^2] \exp[-(\sqrt{8}\sigma_{\xi,i} r_i)^2] & \text{(Mexican Hat)} \end{cases}$$
$$\forall \xi \in \{x, y, z\} \quad \& \quad \forall i \in \{1, \cdots, N_\mathrm{e}\} \tag{2}$$

with

$$r_i = r_i(\mathbf{x}, t) = (x - x_{o,i} - u_\infty t)^2 + (y - y_{o,i} - v_\infty t)^2 + (z - z_{o,i} - w_\infty t)^2 \tag{3}$$

where $(\epsilon_x, \epsilon_y, \epsilon_z)$ is an amplitude vector to determine the directional strength of the eddies; $(\sigma_x, \sigma_y, \sigma_z)$ is a set of constants that determines the size of each eddy component; and, $\mathbf{x}_\mathrm{o} = (x_\mathrm{o}, y_\mathrm{o}, z_\mathrm{o})$ is the centre location of an eddy. The subscript $\xi \in \{x, y, z\}$ represents each directional component and $i \in \{1, \cdots, N_\mathrm{e}\}$ is an index to denote each individual eddy. The argument function $r(\mathbf{x}, t)$ indicates that the eddies move downstream with the mean flow $\mathbf{u}_\infty = (u_\infty, v_\infty, w_\infty)$. The Gaussian and Mexican-hat profiles produce various length scales ranging from the eddy diameter all the way down to the grid cell size. The Mexican-hat profile is particularly effective in providing more small scales as shown in Fig. 1.

It is shown in [12] that the arrangement through Eqs. (1) to (3) satisfies the linearised Euler momentum equations and therefore genuinely removes the possibility of causing pressure fluctuations from the synthetic eddies. The divergence-free condition stand-alone is not a sufficient condition for zero pressure fluctuations as mentioned earlier.

3. Creating Realistic 3D Turbulence Based on SEM

One of the major objectives of the present work is to construct a realistic turbulent velocity field that can be used to simulate aerofoil-turbulence interaction noise. Since natural turbulence exhibits randomness in its characteristics, it is reasonable to synthesise the eddies based on random numbers. However, there should be some constraints in place to harness the randomness in such a way that the statistics of the synthetic turbulence resembles that of the natural one. In the present approach, a total of 15 constraint parameters are introduced to control and optimise the overall distribution of random eddies to reproduce von Kármán velocity spectra for homogeneous isotropic turbulence.

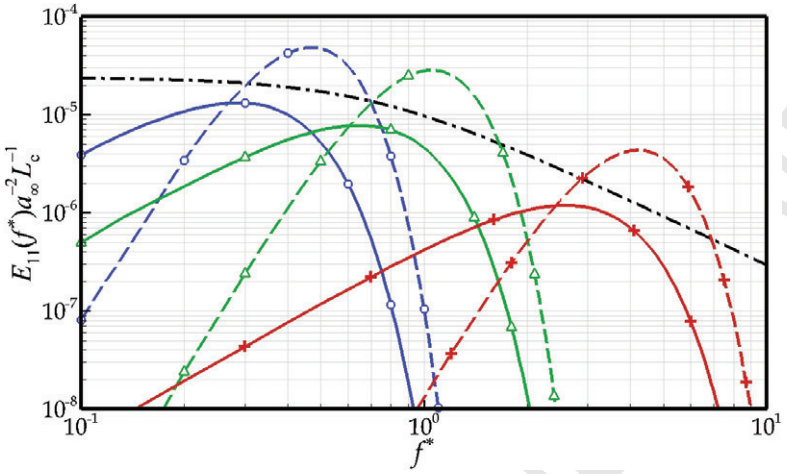

Figure 1: Example profiles of velocity spectra created by individual eddies in different sizes with Gaussian ("——") and Mexican-hat ("– – –") shape functions, compared with a von Kármán spectrum ("–·–" based on 4% integral length scale and 2.5% turbulence intensity). The symbols represent: $R = 0.3$ (○); $R = 0.2$ (△); and, $R = 0.1$ (+). The eddy radius (R) is defined in Sec. 3.1.

3.1. Parametrisation and Definition

The 15 constraint parameters introduced in this paper for use with Eqs. (1) to (3) are defined and listed in Table 1. In the table, the size of an eddy is defined by $R = \sigma^{-1/2}$ (approximate radius) deduced from the shape functions given in Eq. (2). The weighting factor β is introduced to yield a biased eddy distribution towards either the lower (if $\beta > 1$) or the upper bound (if $0 < \beta < 1$) of the eddy size. The superscript "(0)" is used for representing the Gaussian profile and "(1)" for the Mexican Hat, throughout the paper. The details of how these constraint parameters are used for the creation of the synthetic eddies is shown below.

Once the 15 constraint parameters are determined/found (by using an initial guess and subsequent refinements in an iterative manner – see Sec. 3.4), eight independent random numbers are generated and made available for each individual eddy. The random numbers used here are uniformly distributed between zero and one:

$$\varphi_{n,i} \in \mathcal{U}(0,1), \quad \forall i \in \{1, \cdots, N_e\}, \quad \forall n \in \{1, \cdots, 8\} \tag{4}$$

where $\mathcal{U}$ denotes the uniform distribution which facilitates creating a homogeneous turbulence within the virtual eddy box. The generated random

Table 1: Constraint parameters introduced in this paper to optimise synthetic eddies and create realistic turbulence statistics. "G" and "MH" indicating Gaussian and Mexican Hat profiles, respectively as defined in Eq. (2).

Parameters	Definitions
N_e	Total number of eddies created in a virtual eddy box
L_e	Length of the virtual eddy box
α_g	Probability of G-eddies ($1-\alpha_\mathrm{g}$: probability of MH-eddies)
$R^{(0)}_\mathrm{min}, R^{(1)}_\mathrm{min}$	Lower limits in eddy sizes (radii): G (0) and MH (1)
$R^{(0)}_\mathrm{max}, R^{(1)}_\mathrm{max}$	Upper limits in eddy sizes (radii): G (0) and MH (1)
$\beta^{(0)}, \beta^{(1)}$	Weighting for biased eddy distributions: G (0) and MH (1)
$a^{(0)}_x, a^{(1)}_x$	Upper limits in eddy strength in $x-$direction: G (0) and MH (1)
$a^{(0)}_y, a^{(1)}_y$	Upper limits in eddy strength in $y-$direction: G (0) and MH (1)
$a^{(0)}_z, a^{(1)}_z$	Upper limits in eddy strength in $z-$direction: G (0) and MH (1)

numbers are then linked with the constraint parameters to determine the type, size, coordinate and directional strength of each eddy component as follows:

$$m_i = \begin{Bmatrix} 0 & \text{if} & \varphi_{1,i} \le \alpha_\mathrm{g} \\ 1 & \text{if} & \varphi_{1,i} > \alpha_\mathrm{g} \end{Bmatrix}, \quad \forall i \in \{1, \cdots, N_\mathrm{e}\}, \tag{5}$$

$$\begin{pmatrix} R_{x,i} \\ R_{y,i} \\ R_{z,i} \end{pmatrix} = R^{(m_i)}_\mathrm{min} + (R^{(m_i)}_\mathrm{max} - R^{(m_i)}_\mathrm{min}) \begin{pmatrix} \varphi^{\beta(m_i)}_{1,i} \\ \varphi^{\beta(m_i)}_{2,i} \\ \varphi^{\beta(m_i)}_{3,i} \end{pmatrix}, \tag{6}$$

$$(\sigma_{x,i}, \sigma_{y,i}, \sigma_{z,i}) = \left(R^{-2}_{x,i}, R^{-2}_{y,i}, R^{-2}_{z,i}\right), \tag{7}$$

$$x_{o,i} = \begin{Bmatrix} x_\mathrm{ref} - \kappa R_{x,1} & \text{if } i = 1 \\ x_{o,i-1} - \kappa(R_{x,i-1} + R_{x,i}) & \text{if } i \ge 2 \end{Bmatrix} \text{ with } \kappa = L_\mathrm{e} \Big/ \sum_{\ell=1}^{N_\mathrm{e}} 2R_{x,\ell}, \tag{8}$$

$$y_{o,i} = R_{y,i}\left(\varphi_{4,i} - \tfrac{1}{2}\right), \tag{9}$$

$$z_{o,i} = \min(L_z, \hat{L}_z)\left(\varphi_{5,i} - \tfrac{1}{2}\right) \text{ with } \hat{L}_z = 3L_z - 2\max(R_{x,i}, R_{y,i}, R_{z,i}), \tag{10}$$

$$(\epsilon_{x,i}, \epsilon_{y,i}, \epsilon_{z,i}) = \left(a^{(m_i)}_x, a^{(m_i)}_y, a^{(m_i)}_z\right) \cdot (2\varphi_{6,i} - 1, 2\varphi_{7,i} - 1, 2\varphi_{8,i} - 1). \tag{11}$$

Equation (5) selects the type of the eddies between Gaussian ($m = 0$) and Mexican Hat ($m = 1$) depending on the probability factor $\alpha_\mathrm{g} \in [0, 1]$. Equation (6) determines the radii of the eddy components based on the random

numbers $(\varphi_1, \varphi_2, \varphi_3) \in \mathcal{U}(0,1)$ varying from the lower to the upper bounds pre-determined earlier. The exponent (weighting factor) β in Eq. (6) drives the eddy distribution towards the upper bound (large sizes for low frequencies) if $0 < \beta < 1$ or towards the lower bound (small sizes for high frequencies) if $\beta > 1$. The streamwise locations of the eddies (x_o) are given by Eq. (8) in such a way that the distance between any two adjacent eddies is proportional to the sum of their x-component radii and that all the eddies are contained in the specified length (L_e) of the virtual eddy box. The coordinate x_ref represents the forefront position of the virtual eddy box (to be clarified in Sec. 4). Equations (9) and (10) determines the vertical and spanwise locations of the eddies, where $|y_\mathrm{o}| \leq R_y/2$ and $|z_\mathrm{o}| \leq L_z/2$ (L_z: the span of the domain). This means that the cross-section area of the box is $A_\mathrm{e} = 3R_\mathrm{max}L_z$ that is required in Eq. (1). The origin of the coordinate system $(x, y, z) = (0, 0, 0)$ always refers to the geometric centre of the body (aerofoil) in this paper. The buffer variable $\hat{L}_z$ in Eq. (10) is introduced to keep the influence of an eddy within $|z| \leq 3L_z/2$ and therefore an efficient construction of a spanwise periodic boundary condition of class C^∞ is allowed (see Sec. 3.2). This also means that the size of the largest eddy (R_max) should be smaller than $3L_z/2$. Lastly, Equation (11) indicates that the directional amplitude and its sign may change randomly within the specified lower and upper limits.

One of the advantages in the present SEM is that the stream of the convecting eddies is narrowed around the body of interest (aerofoil) and its vicinity only, where the size of the stream is controlled by Eq. (9), i.e. $y \in [-1.5R_\mathrm{max}, 1.5R_\mathrm{max}]$. This helps to minimise the computational overhead in calculating/storing the inflow velocity signals; removes the necessity to lay out fine meshes in the far field; and, also keeps the far field undisturbed by the flow turbulence for clean aeroacoustic environment.

3.2. Periodic Boundary Conditions

One of the most common boundary conditions used in 3D simulations of aerofoil flows is periodic conditions across the spanwise boundaries. A basic approach to impose such a periodic boundary condition (PBC) when creating a synthetic turbulence field is to use a blending technique, e.g. $f(z) = g(z) + g(L - z)$ for $z \in [0, L]$ which satisfies $f^{(2n)}(0) = f^{(2n)}(L)$ for $n \geq 0$ but $f^{(2n+1)}(0) \neq f^{(2n+1)}(L)$. The discontinuities (particularly of the first order) may become a critical issue in aeroacoustic simulations where the order of accuracy of the solution needs to be high (normally fourth order or higher). Ideally, C^∞-continuity in the PBC will remove the possibility

of causing dispersive errors (eventually radiating as spurious noise) when numerical differentiation (e.g. a seven-point-stencil central difference) takes place across the boundaries.

In this paper, a spanwise PBC with C^∞-continuity is proposed to ensure an artefact-free sound field as a result of the current simulation of aerofoil-turbulence interaction. The proposed strategy to construct the PBC is that the virtual box of eddies is duplicated and repeated on the left- as well as the right-hand side of the original box. The induced velocity profile across the centre box becomes periodic due to the recurrence of eddy distribution across the span. This process does not affect the divergence-free condition which is inherently satisfied for each individual eddy. The spanwise PBC is created by using the following equation:

$$\mathbf{\Psi}_{\mathrm{PBC}}(\mathbf{x},t) = \mathbf{\Psi}(\mathbf{x}-L_z\mathbf{e}_z,t) + \mathbf{\Psi}(\mathbf{x},t) + \mathbf{\Psi}(\mathbf{x}+L_z\mathbf{e}_z,t) \tag{12}$$

where the original vector potential $\mathbf{\Psi}(\mathbf{x},t)$ has already been given by Eqs. (1) to (3) and through the procedure described in Sec. 3.1. The spanwise domain is $z \in [-L_z/2, L_z/2]$. Equation (12) indicates that the number of eddies and the size of virtual eddy box triple in order to implement the current spanwise PBC. As described in Sec. 3.1 based on Eq. (10), the size of the largest eddy ($R_{\max}$) is limited to $3L_z/2$ with its centre located at the middle of the span in order to prevent an eddy in the centre box from reaching beyond the far sides of the neighbouring boxes. This leads to:

$$\mathbf{\Psi}\big|_{z=\pm\frac{3}{2}L_z} = \left.\frac{\partial^n \mathbf{\Psi}}{\partial z^n}\right|_{z=\pm\frac{3}{2}L_z} = 0, \quad \forall n = 1,2,3,\cdots \tag{13}$$

and therefore,

$$\mathbf{\Psi}_{\mathrm{PBC}}\big|_{z=\pm\frac{L_z}{2}} = \mathbf{\Psi}\big|_{z=-\frac{L_z}{2}} + \mathbf{\Psi}\big|_{z=\frac{L_z}{2}}\,, \tag{14}$$

$$\left.\frac{\partial^n \mathbf{\Psi}_{\mathrm{PBC}}}{\partial z^n}\right|_{z=\pm\frac{L_z}{2}} = \left.\frac{\partial^n \mathbf{\Psi}}{\partial z^n}\right|_{z=-\frac{L_z}{2}} + \left.\frac{\partial^n \mathbf{\Psi}}{\partial z^n}\right|_{z=\frac{L_z}{2}} \quad \forall n \geq 1, \tag{15}$$

which proves the C^∞-continuity of the proposed PBC across the spanwise boundaries.

The same approach may be used in order to create temporal periodicity in the velocity signal. Duplicating the distribution of the eddies in the streamwise direction results in a periodic time signal. A similar approach has been used by Lund et al. [16]. The periodic time signal is beneficial in terms of

keeping the computational cost (both CPU time and data storage) at a reasonable level and also allowing for efficient post-processing of the simulation data associated particularly with Fourier transformation routines.

3.3. Optimisation Target: von Kármán Velocity Spectra

Based on the arrangements described above, an optimisation of the 15 constraint parameters (defined in Sec. 3.1) is performed in order to construct realistic von Kármán velocity spectra as a result. The von Kármán spectra for a homogeneous isotropic velocity field are given by [17]:

$$\Phi_{ij}(\mathbf{k}) = A(k)\left(\delta_{ij} - \frac{k_i k_j}{k^2}\right), \quad \forall i \in \{1,2,3\} \ \ \& \ \ \forall j \in \{1,2,3\} \tag{16}$$

with

$$A(k) = \frac{55 L_0^5 \Gamma(5/6) u_{\mathrm{rms}}'^2 k^2}{36\pi^{3/2}\Gamma(1/3)\left(1+L_0^2 k^2\right)^{17/6}} \ \ \& \ \ L_0 = \frac{\Gamma(1/3)}{\sqrt{\pi}\Gamma(5/6)} L_{\mathrm{t}} \tag{17}$$

where k_i's are wavenumbers, $k^2 = k_i k_i$, $u_{\mathrm{rms}}'^2 = \overline{u_i' u_i'}/3$, Γ is the gamma function and L_{t} is the integral length scale. The power spectral density function for each velocity component can be calculated by

$$E_{11}^{\mathrm{VK}}(k_1) = 2\iint_{-\infty}^{\infty} \Phi_{11}(\mathbf{k}) dk_2 dk_3, \tag{18}$$

$$E_{22}^{\mathrm{VK}}(k_1) = E_{33}^{\mathrm{VK}}(k_1) = \frac{1}{2}\left(E_{11}^{\mathrm{VK}}(k_1) - k_1 \frac{dE_{11}^{\mathrm{VK}}}{dk_1}\right) \tag{19}$$

which yields

$$E_{11}^{\mathrm{VK}}(k_1) = \frac{u_{\mathrm{rms}}'^2 L_{\mathrm{t}}}{\pi\left(1+L_0^2 k_1^2\right)^{5/6}}, \ \ E_{22,33}^{\mathrm{VK}}(k_1) = \frac{u_{\mathrm{rms}}'^2 L_{\mathrm{t}}\left(3+8L_0^2 k_1^2\right)}{6\pi\left(1+L_0^2 k_1^2\right)^{11/6}} \tag{20}$$

for the longitudinal and transverse velocity spectra, respectively. The superscript "VK" denotes "von Kármán". In this paper $E_{ii}^{\mathrm{VK}}(k_1)$ are multiplied by a factor of 2 to convert them to one-sided spectra. In addition, the spectra are transformed into a dimensionless frequency domain via:

$$f^* = \frac{f L_{\mathrm{c}}}{a_\infty} = \frac{k_1}{2\pi} L_{\mathrm{c}} M_\infty. \tag{21}$$

where L_c is the reference length in this paper (aerofoil chord) and M_∞ is the free-stream Mach number.

In this work, the velocity spectra required at the position where an aerofoil's leading-edge would be located are characterised by $u'_\mathrm{rms}/u_\infty = 0.025$ (2.5% turbulence intensity) and $L_\mathrm{t}/L_\mathrm{c} = 0.04$. These data were obtained from an experimental measurement of grid turbulence carried out in an anechoic wind tunnel at the Institute of Sound and Vibration Research (ISVR) of the University of Southampton. The wind speed was $u_\infty = 80\,\mathrm{m/s}$ ($M_\infty = 0.24$) and the aerofoil chord was $L_\mathrm{c} = 15\,\mathrm{cm}$ (hence $Re_\infty = 8.6 \times 10^5$ based on u_∞ and L_c). It was confirmed that the measured velocity spectra matched very well with the corresponding von Kármán spectra [18]. Since the synthetic turbulence is generated at the inflow boundary, the target velocity spectra at the inlet should be different from those at the aerofoil's leading-edge position. Under the present numerical set-up, $u'_\mathrm{rms}/u_\infty = 0.04$ (4% turbulence intensity) and $L_\mathrm{t}/L_\mathrm{c} = 0.04$ are set as the target to achieve at the inlet, which is found to lead to the desired experimental condition at the aerofoil's leading-edge position.

3.4. Optimising Eddy Constraint Parameters

Once the target von Kármán velocity spectra are identified, an optimisation of the 15 constraint parameters:

$$\boldsymbol{\phi} = (N_\mathrm{e}, L_\mathrm{e}, \alpha_\mathrm{g}, R^{(0)}_\mathrm{min}, R^{(0)}_\mathrm{max}, R^{(1)}_\mathrm{min}, R^{(1)}_\mathrm{max}, \beta^{(0)}, \beta^{(1)}, a^{(0)}_x, a^{(0)}_y, a^{(0)}_z, a^{(1)}_x, a^{(1)}_y, a^{(1)}_z) \tag{22}$$

is carried out in order to find a local minimum of the following L_∞-norm error function:

$$\mathscr{E}(\boldsymbol{\phi}) = \max_{i=1}^{3} \max_{f^*=f^*_\mathrm{a}}^{f^*_\mathrm{b}} \left| \log_{10} \frac{\langle E_{ii}(f^*)\rangle}{E^\mathrm{VK}_{ii}(f^*)} \right| \tag{23}$$

with

$$\langle E_{ii}(f^*)\rangle = \frac{1}{L_z} \int_{-L_z/2}^{L_z/2} E_{ii}(f^*, z)\big|_{(x,y)=(x_\mathrm{min},0)} dz \tag{24}$$

where $f^* \in [f^*_\mathrm{a}, f^*_\mathrm{b}]$ is the range of frequencies considered in the optimisation. In the current optimisation platform, $f^*_\mathrm{a} = 0.1$ and $f^*_\mathrm{b} = 2.5$ are selected, which correspond to 228Hz and 5690Hz, respectively. The numerical spectra $E_{ii}(f^*, \mathbf{x})$ are calculated from the vector potential $\boldsymbol{\Psi}_\mathrm{PBC}$ given by Eq. (12) that includes both the spanwise and temporal periodic conditions. The error

function $\mathscr{E}(\boldsymbol{\phi})$ returns the largest deviation of the spanwise-averaged numerical spectra from the desired von Kármán ones within the specified frequency range.

In this work, the number of eddies and the length of the virtual eddy box are fixed at $N_\mathrm{e} = 300$ and $L_\mathrm{e} = 5.76L_\mathrm{c}$ for computational efficiency although more eddies and a longer box would help improving the result. The time required for an eddy to travel the distance of L_e is therefore (in a dimensionless form) $a_\infty t/L_\mathrm{c} = M_\infty^{-1} L_\mathrm{e}/L_\mathrm{c} = 24$, which is sufficiently long for a statistical analysis. In the meantime, the smallest eddy size relative to the aerofoil chord ($R_\mathrm{min}^{(1)}/L_\mathrm{c}$) is limited at an affordable level (0.1 in this work) since the grid density at the inflow boundary should be sufficiently high to resolve the smallest eddy. The rest of the constraint parameters are determined when a gradient-based optimisation technique converges to a local minimum $\partial\mathscr{E}/\partial\phi_i = 0$ (if failing to find the global minimum) of the error function in Eq. (23). The gradient-based optimisation is accelerated by adopting Genetic Algorithm (via MATLAB Toolbox) and therefore each cycle of the optimisation is completed within a reasonable length of time. The optimisation is repeated with updating the random numbers $(\varphi_1, \cdots, \varphi_8)$ required in Eq. (4) until the most satisfactory velocity spectra are obtained. It should be noted that Equation (23) is calculated on the horizontal plane ($y = 0$) that covers the aerofoil planform area, and the Ensemble average of the spectra over the span is taken into account in the iterative optimisation process in order to get sufficiently uniform spectra across the span. The length of span is fixed at $L_z/L_\mathrm{c} = 0.26$ in the present work (see Sec. 6 for the reason). The resulting constraint parameters revealed at the completion of the optimisation are listed in Table 2.

The resulting velocity signals and their spanwise-averaged spectra obtained are plotted in Fig. 2 and Fig. 3 for each velocity component. It is shown that the synthetic turbulence spectra are overall in good agreement with the corresponding von Kármán ones across the frequency range $f^* \in [0.1, 2.5]$ although the streamwise component (u') exhibits a fast decay compared to the vertical (v') and spanwise (w') ones (v' being mainly responsible for the source mechanism of aerofoil-turbulence interaction noise). The fast decay in the streamwise component has already been expected from Fig. 2 where the u' signal shows significantly less frequent fluctuations than those of v' and w'. The decay from the von Kármán spectra can be delayed if more plentiful eddies in smaller sizes are employed, which leads to increased cost in actual simulations due to finer meshes required to resolve the small-

Table 2: Optimised constraint parameters for Eqs. (5) to (11) with spanwise periodic boundary condition based on Eq. (12) and $L_z/L_\mathrm{c} = 0.26$, in order to obtain von Kármán velocity spectra at inflow boundary for $M_\infty = 0.24$, $u'_\mathrm{rms}/u_\infty = 0.04$ and $L_\mathrm{t}/L_\mathrm{c} = 0.04$.

Constraint Parameters	Optimised Values
N_e	300 (fixed)
$L_\mathrm{e}/L_\mathrm{c}$	5.76 (fixed)
α_g	0.45087254
$R^{(0)}_\mathrm{min}/L_\mathrm{c}$	0.14648081
$R^{(0)}_\mathrm{max}/L_\mathrm{c}$	0.30203081
$R^{(1)}_\mathrm{min}/L_\mathrm{c}$	0.1 (limited)
$R^{(1)}_\mathrm{max}/L_\mathrm{c}$	0.19325727
$\beta^{(0)}$	0.54655705
$\beta^{(1)}$	2.12271470
$a_x^{(0)}$	0.01509330
$a_y^{(0)}$	0.01800811
$a_z^{(0)}$	0.01064091
$a_x^{(1)}$	0.00821648
$a_y^{(1)}$	0.01668158
$a_z^{(1)}$	0.01797790

est eddies. The extra computational effort, however, might not be critically necessary if there is a sufficient space in the computational domain where the turbulence can travel freely and becomes increasingly realistic after a certain distance from the inflow boundary, which is shown in Sec. 5.3. In the meantime, it has been checked that the time signals from the two end-span points are identical as expected due to the spanwise periodic condition imposed by Eq. (12).

It should be noted that all the spectra are calculated based on periodic time signals – with the period of $T_{\mathrm{P}}^{*} = (L_{\mathrm{e}}/L_{\mathrm{c}})/M_{\infty} = 24$ – created by the temporal periodic condition mentioned in Sec. 3.2. The frequency of the periodic turbulence ($f_{\mathrm{P}}^{*} = 1/24 = 0.04167$) is not far from the lowest eddy frequency ($f_{\mathrm{a}}^{*} = 0.1$ set in the current optimisation) albeit still lower by a factor of two. The value of f_{P}^{*} can be reduced by extending the length of the virtual eddy box and allocating more eddies in it, which requires a higher computational cost. In the current simulation (aerofoil-turbulence interaction), the physics of interest (noise reduction due to a geometric change) takes place at a much higher frequency ($f^{*} > 1$). Therefore, the authors considered that the current value of f_{P}^{*} was adequate in this particular case. However, a more careful consideration will be necessary if a generic flow turbulence is studied where much broader spectra are of interest.

4. Governing Equations and Sponge Layers

This section describes the governing equations that are used for the present simulation of aerofoil-turbulence interaction noise and the sponge-layer technique for absorbing spurious wave reflections as well as injecting the synthetic turbulence into the domain through the inflow boundary. The present governing equations are full 3D compressible Euler equations in a conservative form transformed into a generalised coordinate system:

$$\frac{\partial(\mathbf{Q}/J)}{\partial t} + \frac{\partial(\mathbf{E}/J)}{\partial \xi} + \frac{\partial(\mathbf{F}/J)}{\partial \eta} + \frac{\partial(\mathbf{G}/J)}{\partial \zeta} = -\frac{a_{\infty}}{L_{\mathrm{c}}}\frac{\mathbf{S}}{J} \tag{25}$$

where the vectors of conservative variables and fluxes are

$$\mathbf{Q} = \begin{pmatrix} \rho \\ \rho u \\ \rho v \\ \rho w \\ \rho e_{\mathrm{t}} \end{pmatrix}, \mathbf{E} = \begin{pmatrix} \rho U \\ \rho u U + \xi_x p \\ \rho v U + \xi_y p \\ \rho w U + \xi_z p \\ (\rho e_{\mathrm{t}} + p) U \end{pmatrix}, \mathbf{F} = \begin{pmatrix} \rho V \\ \rho u V + \eta_x p \\ \rho v V + \eta_y p \\ \rho w V + \eta_z p \\ (\rho e_{\mathrm{t}} + p) V \end{pmatrix}, \mathbf{G} = \begin{pmatrix} \rho W \\ \rho u W + \zeta_x p \\ \rho v W + \zeta_y p \\ \rho w W + \zeta_z p \\ (\rho e_{\mathrm{t}} + p) W \end{pmatrix} \tag{26}$$

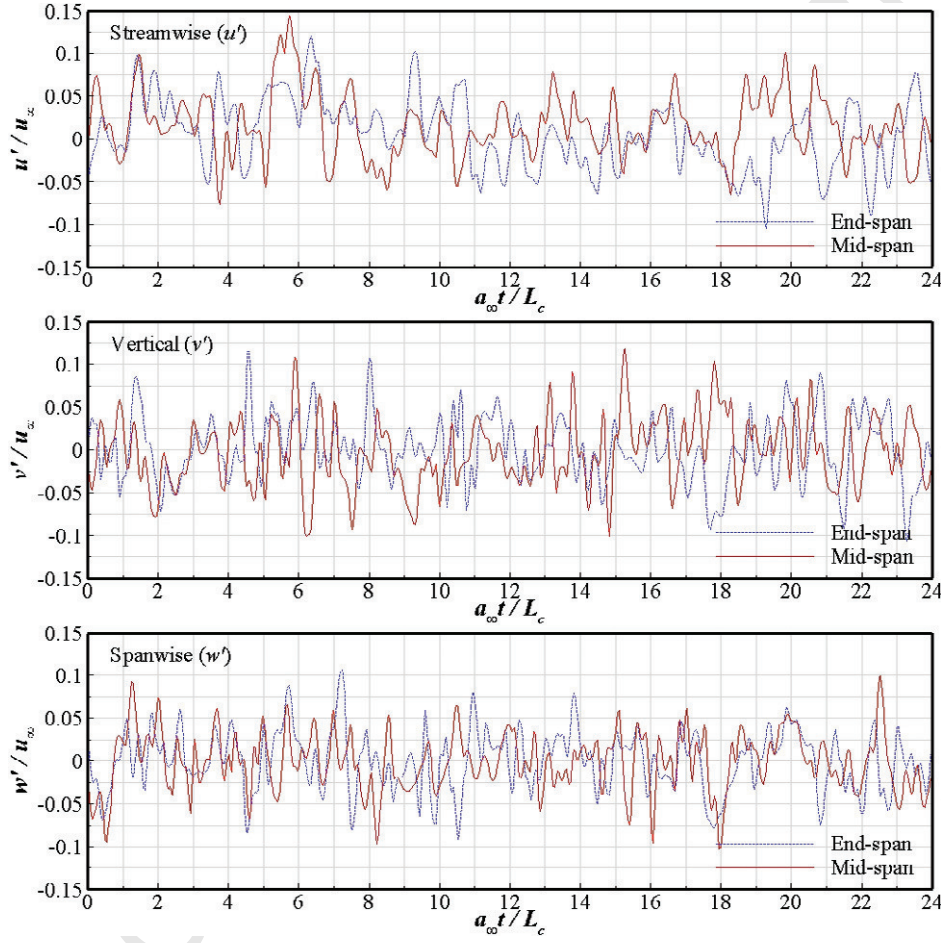

Figure 2: Synthetic turbulent velocity signals obtained at $(x, y) = (x_{\min}, 0)$ to be imposed via inflow boundary conditions. Calculation of the signals based on the parameters listed in Table 2. Plots for two different spanwise locations: mid-span ($z = 0$) and end-span ($z = \pm L_z/2$).

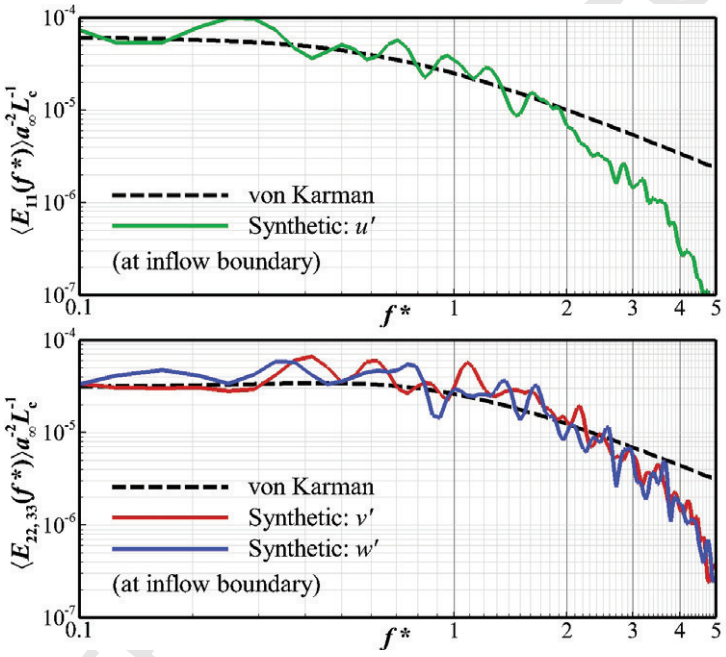

Figure 3: Spanwise-averaged velocity spectra of the synthetic turbulence obtained at the inflow boundary $(x, y) = (x_{\min}, 0)$ based on the parameters listed in Table 2, in comparison with the corresponding von Kármán spectra for $M_\infty = 0.24$, $u'_{\mathrm{rms}}/u_\infty = 0.04$ and $L_{\mathrm{t}}/L_{\mathrm{c}} = 0.04$.

with the internal energy, the contravariant velocities, the coordinate transformation metrics and Jacobian given by

$$
\begin{aligned}
e_\mathrm{t} &= \frac{p}{(\gamma-1)\rho} + \frac{1}{2}(u^2+v^2+w^2),\ (U,V,W)^T = \underline{\mathbf{A}}^{-1}(u,v,w)^T, \\
\underline{\mathbf{A}}^{-1} &= \begin{pmatrix} \xi_x & \xi_y & \xi_z \\ \eta_x & \eta_y & \eta_z \\ \zeta_x & \zeta_y & \zeta_z \end{pmatrix},\ J = |\underline{\mathbf{A}}|^{-1} \quad \text{where } \underline{\mathbf{A}} = \left[\frac{\partial(x,y,z)}{\partial(\xi,\eta,\zeta)}\right].
\end{aligned}
\tag{27}
$$

The additional terms on the right-hand side of Eq. (25) for the sponge layers suggested in [13, 14] are

$$
\mathbf{S} = \begin{cases} \sigma_\mathrm{s}(x,y) \begin{pmatrix} \rho-\rho_\infty \\ \lambda_\mathrm{s}(x)\rho(u-u_\mathrm{target}) \\ \lambda_\mathrm{s}(x)\rho(v-v_\mathrm{target}) \\ \lambda_\mathrm{s}(x)\rho(w-w_\mathrm{target}) \\ p-p_\infty \end{pmatrix} & \text{for} \quad \mathbf{x} \in \Omega_\mathrm{sponge} \\ \mathbf{0} & \text{for} \quad \mathbf{x} \in \Omega_\mathrm{physical} \end{cases}
\tag{28}
$$

with

$$
\sigma_\mathrm{s}(x,y) = \frac{\sigma_\mathrm{o}}{2}(1+\cos[\pi\mathcal{A}(x)\mathcal{B}(y)]), \tag{29}
$$

$$
\mathcal{A}(x) = 1 - \max\left[(x_\mathrm{a}-x)/(x_\mathrm{a}-x_\mathrm{min}),0\right] - \max\left[(x-x_\mathrm{b})/(x_\mathrm{max}-x_\mathrm{b}),0\right],
$$

$$
\mathcal{B}(x) = 1 - \max\left[(y_\mathrm{a}-y)/(y_\mathrm{a}-y_\mathrm{min}),0\right] - \max\left[(y-y_\mathrm{b})/(y_\mathrm{max}-y_\mathrm{b}),0\right],
$$

and

$$
\lambda_\mathrm{s}(x) = (1+\delta)[1-\tanh(x/L_\mathrm{c})]+1 \quad \text{with} \quad \delta = \min[2M_\infty/(1+M_\infty),1] \tag{30}
$$

where $\Omega_\mathrm{physical} = \{\mathbf{x}\,|\,x \in [x_\mathrm{a},x_\mathrm{b}], y \in [y_\mathrm{a},y_\mathrm{b}], z \in [-\frac{1}{2}L_z,\frac{1}{2}L_z]\}$ defines a physical domain in which meaningful simulation data are obtained, and the rest of the domain is used as a sponge layer ($\Omega_\mathrm{sponge} = \Omega_\infty - \Omega_\mathrm{physical}$) surrounding the physical domain. For the present aerofoil-turbulence interaction simulation, $x_\mathrm{a} = -5L_\mathrm{c}$, $x_\mathrm{b} = 6L_\mathrm{c}$ and $y_\mathrm{a} = -y_\mathrm{b} = 5L_\mathrm{c}$ are selected and the entire domain is $\Omega_\infty = \{\mathbf{x}\,|\,x/L_\mathrm{c} \in [-7,11], y/L_\mathrm{c} \in [-7,7], z/L_\mathrm{c} \in [-0.13,0.13]\}$. The current computational domain set-up is shown in Sec. 5 (see Fig. 4). The overall sponge coefficient is set to $\sigma_\mathrm{o} = 3$ in Eq. (29). Details about the sponge-layer technique can be found in [13, 14].

The target velocity field for Eq. (28) in the sponge layer is specified by

$$
\mathbf{u}_\mathrm{target}(\mathbf{x},t) = \mathbf{u}_\infty + H(\mathbf{x})\nabla\times\mathbf{\Psi}_\mathrm{PBC}(\mathbf{x},t) \quad \text{for} \quad \mathbf{x} \in \Omega_\mathrm{sponge} \tag{31}
$$

where the heavyside step function that is switched on in the zone of eddy production is defined by

$$H(\mathbf{x}) = \begin{cases} 1 & \text{for} \quad \mathbf{x} \in \Omega_{\text{eddy}} \\ 0 & \text{for} \quad \mathbf{x} \in \Omega_{\text{sponge}} - \Omega_{\text{eddy}} \end{cases} \tag{32}$$

and the zone of the eddy production is given by

$$\Omega_{\text{eddy}} = \{\mathbf{x} \,|\, x \in [x_{\min}, x_{\text{a}}] \;\&\; y \in [-2R_{\max}, 2R_{\max}]\}. \tag{33}$$

Therefore a small portion of the sponge layer ($\Omega_{\text{eddy}} \subset \Omega_{\text{sponge}}$) is used to inject the inflow turbulence into the domain. The height of Ω_{eddy} is set to $4R_{\max}$ which is larger than that of A_{e} ($3R_{\max}$ as indicated in Sec. 3.1) in order to ascertain smooth transition between Ω_{eddy} and Ω_{sponge}. Considering the vertical distribution (y-coordinates) of the eddies given by Eq. (9), the top and bottom boundaries of Ω_{eddy} are sufficiently distant from the eddies, where the induced velocity converges to zero, hence smoothly restoring the uniform mean flow $\mathbf{u}_\infty$ without discontinuity in Eqs. (28) and (31).

Following up on Sec. 3.1, the parameter x_{ref} in Eq. (8) is set to $x_{\text{ref}} = \frac{1}{2}(x_{\min} + x_{\text{a}} + L_{\text{e}})$ so that the centre of the virtual eddy box is located at the centre of Ω_{eddy} at the start of the simulation. The time signal of the eddy-induced velocity is obtained at each grid point in Ω_{eddy} as the virtual eddy box moves downstream with the mean flow. In practice, two different options of calculating the induced velocity may be considered: 1) instantaneous values are calculated along with the simulation at each and every time step (and sub-iterative stages between the time steps as necessary); and, 2) a full-length time signal with a reasonable time interval is pre-calculated and stored in a separate binary datafile before the simulation starts which can be accessed fast whenever required. Since Eq. (2) involves exponential operators that are slow in execution, the second option is recommended over the first one although it requires an additional (but not exhaustive) local interpolation routine. The second option is also beneficial as the same datafile (once created) can be re-used for repeating simulations as far as the meshes remain unchanged inside Ω_{eddy}. In the current computing set-up described in Sec. 5.1, the wall-clock time taken to create the time signal datafile based on the second option is typically under an hour without employing any extra parallelisation or GPU acceleration techniques which might significantly reduce the pre-processing time.

5. Numerical Test of the New Synthetic Turbulence

In this section, the proposed method of 3D synthetic turbulence generation is numerically implemented to test its genuine feasibility for direct aeroacoustic simulations. The primary viewpoint in this section is the level of spurious noise that may develop from the synthetic eddies injected into the computational domain. The eddy vector potential given by Eq. (1) is an exact solution to the linearised Euler equations free of entropy and acoustic perturbations [12]. Applying it to the full nonlinear Euler equations may give rise to the entropy/acoustic waves (spurious noise) in the present simulations. Also, there is a certain level of dispersive errors existing in the numerical solution that may radiate as spurious noise as well. The objectives in this section are 1) to ensure that the level of spurious noise is sufficiently low and 2) to find a suitable grid resolution to achieve this. In the meantime, it is checked if the statistics of the synthetic turbulence obtained inside the computational domain matches well with the desired von Kármán spectra at the position where an aerofoil is to be placed in the next section.

5.1. High-order Computational Aeroacoustic Simulation

In this work, the full 3D Euler equations with the sponge layers described in Sec. 4 are solved by using high-order accurate numerical methods specifically developed for aeroacoustic simulations on structured grids. The flux derivatives in space are calculated based on fourth-order pentadiagonal compact finite-difference schemes with seven-point stencils [19]. Explicit time advancing of the numerical solution is carried out by using the classical fourth-order Runge-Kutta scheme with the CFL number of 0.95. The numerical stability is maintained by implementing sixth-order pentadiagonal compact filters for which the cut-off wavenumber (normalised by the grid spacing) is set to 0.87π [20]. In addition to the sponge layers used, characteristics-based non-reflecting boundary conditions [21] are applied at the far boundaries in order to prevent any outgoing waves from returning to the computational domain. Periodic conditions are used across the spanwise boundary planes as indicated earlier.

The computation is massively parallelised via domain decomposition and message passing interface (MPI) approaches. The compact finite-difference schemes and filters used are implicit in space due to the inversion of pentadiagonal matrices involved, which requires a precise and efficient technique for the parallelisation in order to avoid numerical artefacts that may appear

at the subdomain boundaries. A recent parallelisation approach based on quasi-disjoint matrix systems [22] offering super-linear scalability is used in the present paper. The entire domain Ω_∞ indicated in Sec. 4 is decomposed and distributed onto 312 separate computing nodes/subdomains ($26 \times 12 \times 1$ in the streamwise, vertical and spanwise directions, respectively). This parallel computing set-up is maintained throughout the paper.

A snapshot of the resulting pressure (p'/p_∞) and velocity (v'/a_∞) fields obtained at the end of a test calculation is shown in Fig. 4. The calculation ran up to $t^* = a_\infty t/L_\mathrm{c} = 80$ which is sufficiently long to reach a fully developed flow (after a transient phase from the initial condition) and to obtain a statistically stationary result when the time signals are sampled for the duration of $T_\mathrm{P}^* = 24$ indicated at the end of Sec. 3.4. The present synthetic turbulence described in Figs. 2 and 3 is created and injected into the ambient field through the zone of eddy production Ω_eddy. The calculation is performed on a stretched grid with rectangular meshes. The smallest meshes with the size of $\Delta x = \Delta y = 0.008333 L_\mathrm{c}$ (with Δz depending on the number of cells used in the spanwise direction) are located at $(x, y) = (\pm 0.5 L_\mathrm{c}, 0)$ where an aerofoil will be placed in Sec. 6. The meshes are gradually stretched within the central (near-field) domain and kept almost uniform in the mid- and far-field domain (except the downstream sponge zone). A close-up view on the synthetic turbulence is presented in Fig. 5 based on iso-contour surfaces of vorticity magnitude, where entirely three-dimensional turbulence structures are displayed. It shows randomly coiling worm-like structures which characterise homogeneous isotropic turbulence as reported by Chakraborty *et al.* [23].

5.2. Spurious Noise Level

It is shown in Fig. 4 that the resulting synthetic turbulence exhibits very little influence in the far field even at the low contour levels. In order to examine the level of spurious noise that may exist at the far field, the time history of pressure fluctuations is recorded at an observer point $\mathbf{x} = (0, 5L_\mathrm{c}, 0)$ (point A denoted in Fig. 4) and the normalised power spectral density (PSD) of the sound pressure level (SPL) is calculated as

$$S_{pp}(f_n) = \frac{2}{p_\infty^2} \int_{-T/2}^{T/2} \overline{p'(t)p'(t+\tau)} e^{-2\pi i f_n \tau} d\tau = \frac{2}{T p_\infty^2} P(f_n) \tilde{P}(f_n) \qquad (34)$$

where $f_n = n/T$ (n is a positive integer). The overline and the tilde denote time averaging and complex conjugate, respectively. The PSD of the periodic

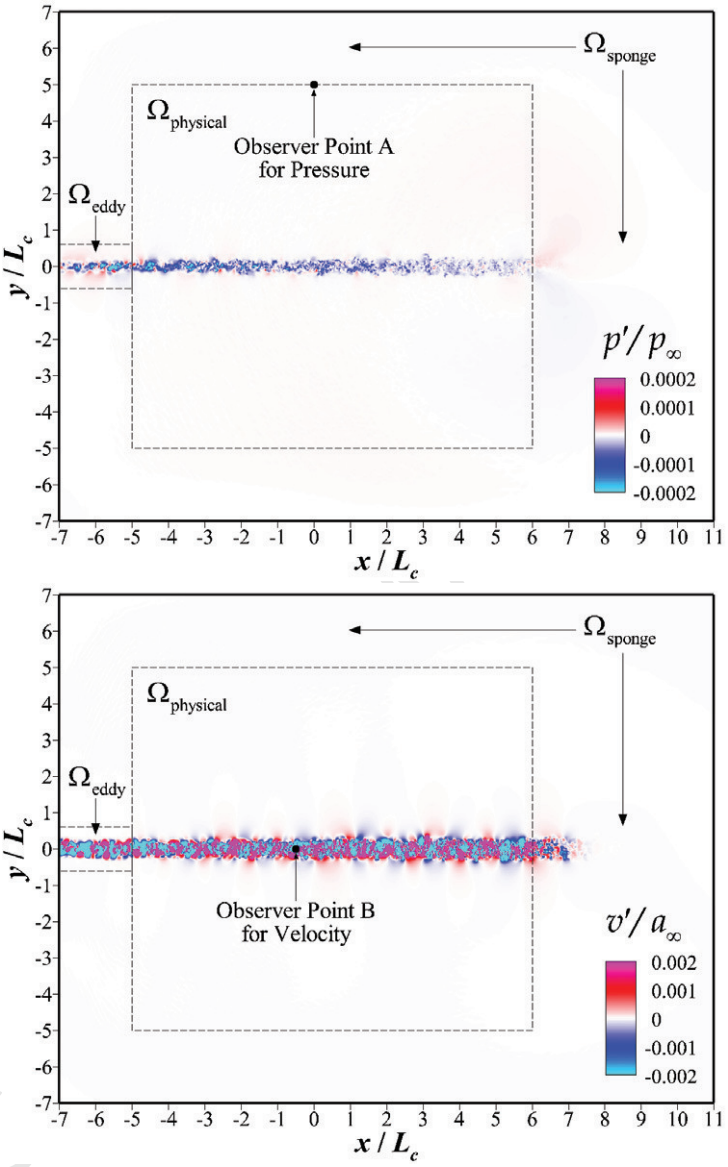

Figure 4: Contour plots of perturbed pressure (top) and velocity (bottom) fields due to the turbulent stream convecting downstream (left to right) at $M_\infty = 0.24$ in an ambient field. Snapshots obtained at $a_\infty t/L_c = 80$ and taken from an $xy-$plane at the mid-span ($z = 0$). Synthetic turbulence generated within Ω_{eddy} based on 4% intensity ($u'_{\text{rms}}/u_\infty = 0.04$) and 4% length scale ($L_t/L_c = 0.04$) as designed in Sec. 3.4. A total of 24,710,400 grid cells used in 3D domain. Contour levels up to $\pm 2\times10^{-4}$ for pressure and $\pm 2\times10^{-3}$ for velocity.

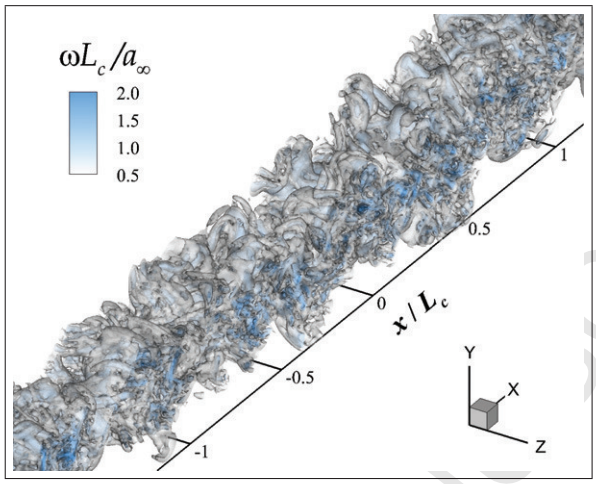

Figure 5: Iso-contour surfaces of normalised vorticity magnitude $\omega L_c/a_\infty$ ($\omega = |\nabla \times \mathbf{u}|$) obtained from the result shown in Fig. 4. A close-up view around the centre of the domain where an aerofoil is to be placed (see Sec. 6). Four contour levels from 0.5 to 2.

pressure signal is obtained by

$$P(f_n) = \int_{-T/2}^{T/2} p'(t) e^{-2\pi i f_n t} dt. \tag{35}$$

The factor $2/T$ in Eq. (34) is required to achieve $\int_0^\infty S_{pp}(f)df = \overline{p'^2}/p_\infty^2$.

The resulting sound pressure spectra are shown in Fig. 6 and the sound pressure level is listed in Table 3. Four different cases with various grid resolution are tested in order to find out the minimum number of grid cells required to resolve the smallest eddies injected into the domain keeping the spurious noise at a tolerable level. The total number of grid cells used for each case is listed Table 4. It is clear from Table 3 and Fig. 6 that the spurious noise decreases as the grid resolution increases, particularly in the mid-to-high frequency range. The grid-dependency test does suggest that about 10 cells across $R_{\min}$ is required to keep the level of the spurious noise sufficiently low in the mid-to-high frequency range. Henceforth, this criterion (10 cells/$R_{\min}$, i.e. 100 cells/L_c in Ω_{eddy}) is applied to the simulation of aerofoil-turbulence interaction noise in Sec. 6. This criterion (20 cells per eddy "diameter") is in line with the result of a previous study [22] which indicated that a single vortex would be under-resolved with 12.3 cells and over-resolved with 28.7 cells per its diameter for the same spatial discretization used.

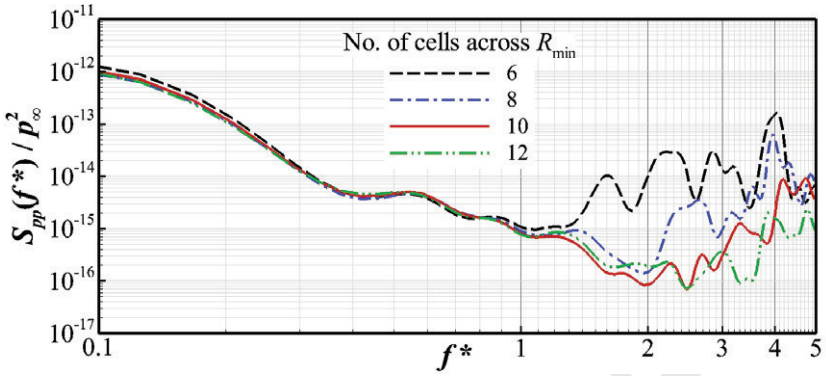

Figure 6: The PSD of spurious noise generated by synthetic turbulence convecting in an ambient domain. Pressure signals obtained at the observer point A shown in Fig. 4. Four different levels of grid resolution used ($R_{\min}$ indicating the radius of the smallest eddy specified in Table 2).

Table 3: The level of spurious noise generated by synthetic turbulence convecting in an ambient domain. Tests with four different levels of grid resolution against the smallest eddy size. Based on pressure signals recorded at the observer point A denoted in Fig. 4.

Minimum number of cells used per smallest eddy's radius ($R_{\min}$)	Resulting spurious noise level ($\overline{p'^2}/p_\infty^2$)
6	5.157×10^{-13} (71.1dB)
8	3.876×10^{-13} (69.9dB)
10	3.701×10^{-13} (69.7dB)
12	3.900×10^{-13} (69.9dB)

Table 4: Total number of cells used in the simulation of convecting synthetic turbulence shown in Fig. 4 for four different levels of grid resolution.

Minimum number of cells used per smallest eddy's radius ($R_{\min}$)	Total number of cells used for the entire domain
6	$5,778,432$ ($912\times396\times16$)
8	$13,039,488$ ($1176\times528\times21$)
10	$24,710,400$ ($1440\times660\times26$)
12	$41,836,608$ ($1704\times792\times31$)

5.3. Mid-domain Velocity Spectra

The synthetic turbulence produced at the inflow boundary region is bound to change due to the interaction between eddies at the integral scale (e.g. vortex dynamics) and eventually develops more realistic turbulence characteristics as it convects downstream. In this work, it is aimed to reproduce the same turbulence statistics at the position (the observer point B at $\mathbf{x} = (-0.5L_c, 0, 0)$ denoted in Fig. 4) where a previous experimental measurement was carried out (mentioned in Sec. 3.3). For this purpose, velocity signals are recorded and their spectra are calculated at the observer point B corresponding to the leading edge of the aerofoil to be located. The resulting spectra are shown in Fig. 7 and they are overall in good agreement with the desired von Kármán ones. Also, it is clear by comparing Figs. 3 and 7 that the spectral bandwidth has expanded to $f^* \in [0.1, 5]$ at the mid domain from $[0.1, 2.5]$ that was obtained at the inflow boundary. The improvement in the u' spectrum is of particular significance. The expanded bandwidth is attributed to the natural development of the turbulence that takes place as it travels a sufficient distance from the inflow boundary. The effectiveness of the proposed synthetic eddy method is successfully demonstrated.

On another note, the success of synthetic turbulence might also be measured based on how fast the turbulence becomes realistic. This type of measure will be much more relevant in the context of internal flows where the distance that the turbulence travels before turning realistic may be a primary factor to determine the length of the computational domain and therefore significantly related to the cost of the simulation.

6. Application to Aerofoil-Turbulence Interaction Noise

In this section, the new synthetic turbulence is applied to the simulation of aerofoil-turbulence interaction (ATI) noise and the results are compared against a well-known theoretical prediction model and existing measurement data from a recent anechoic wind-tunnel experiment. ATI is one of the fundamental source mechanisms of aerofoil noise predominantly generated by surface pressure fluctuations taking place at the leading edge in exchange with rapid distortion of the vorticity field impinging on the aerofoil [24, 25]. As ATI can be regarded as a purely inviscid mechanism [24, 25], the present simulations are based on the Euler equations as described in Sec. 4 and slip wall boundary conditions [26] are imposed on the aerofoil surface. The Euler simulation is also preferred in order to isolate the ATI noise from self-noise

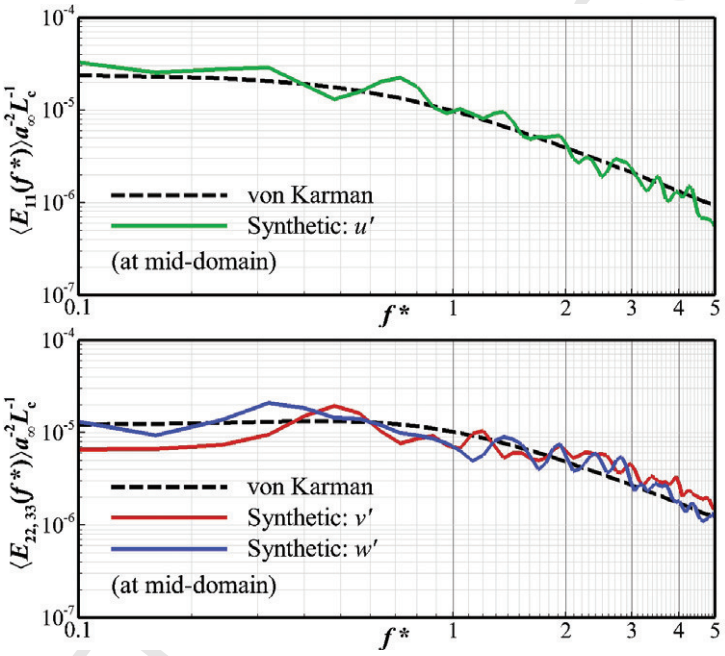

Figure 7: Spanwise-averaged velocity spectra of the evolving turbulence obtained at the observer point B: $(x, y) = (-0.5L_c, 0)$ (denoted in Fig. 4), in comparison with the corresponding von Kármán spectra for $M_\infty = 0.24$, $u'_{\rm rms}/u_\infty = 0.025$ and $L_t/L_c = 0.04$.

components associated with viscous effects, e.g. scattering of boundary-layer vortical disturbances inro sound waves at the trailing edge [27].

For the present work, non-lifting thin aerofoils (with zero thickness) with two different leading-edge profiles are considered: a straight (SLE) and a wavy leading edge (WLE). The latter is based on a sinusoidal function of z (spanwise coordinate) that specifies the local position of the leading edge:

$$x_{\mathrm{LE}}(z) = -\tfrac{1}{2}L_{\mathrm{c}} + h_{\mathrm{LE}} \sin\left[2\pi(z - \tfrac{1}{2}L_z)/\lambda_{\mathrm{LE}}\right] \quad \text{for} \quad z \in [-\tfrac{1}{2}L_z, \tfrac{1}{2}L_z] \tag{36}$$

where h_{LE} and λ_{LE} are the amplitude and the wavelength of the leading-edge profile, respectively. The WLE case is presented in this paper to test and showcase the genuine three-dimensionality of the current approach in both the geometry and the synthetic turbulence. In this paper, $h_{\mathrm{LE}} = 0.067L_{\mathrm{c}}$ and $\lambda_{\mathrm{LE}} = 0.5L_z = 0.13L_{\mathrm{c}}$ are selected as were the case in the counterpart experiment (carried out in the ISVR anechoic wind tunnel mentioned in Sec. 3.3). It has recently been studied by Lau, Haeri and Kim [15] that WLE profiles are effective in reducing ATI noise compared to the SLE case but the existing study relied only on a simple form of vortical gusts (single-frequency velocity excitations). A more comprehensive study based on a realistic 3D turbulence may be achieved by adopting the present SEM approach. It is envisaged that the present result will form an enhanced scope of advanced research associated with ATI noise.

The aerofoil geometries and their surface meshes used in the current simulations are shown in Fig. 8. In both SLE and WLE cases, 660, 120 and 660 cells are used in the upstream; across the chord; and, in the downstream of the aerofoil, respectively. Also, 660 cells are located in the vertical direction (330 above and below the aerofoil each). The total number of cells used is 24,710,400 (with the periodic span covered by 26 cells). This is in fact the same grid set-up used and tested in the previous section for the validation of the synthetic turbulence except that the smallest grid cell size is slightly reduced to $\Delta x = \Delta y = 0.00625L_{\mathrm{c}}$ (with $\Delta z = 0.01L_{\mathrm{c}}$) at the leading and trailing edges. Based on the same solution procedure described in Sec. 5.1, the generation and propagation of ATI noise is successfully simulated and the results are plotted in Fig. 9.

Broadband acoustic response to the impinging turbulence is qualitatively visualised in Fig. 9 where it is clearly shown that strong dipole sound waves are emitted from the leading edge of the aerofoil with the secondary scattering event appearing at the trailing edge. It should be noted that the contour

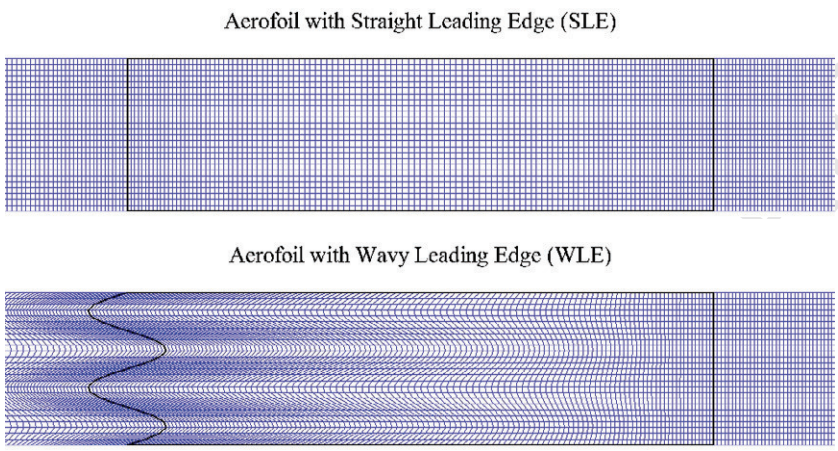

Figure 8: Planform views on two different aerofoil geometries and their surface meshes used in the present study. SLE (top) and WLE (bottom). WLE based on Eq. (36) with $h_{\mathrm{LE}} = 0.067L_{\mathrm{c}}$ and $\lambda_{\mathrm{LE}} = 0.13L_{\mathrm{c}}$ ($L_z = 0.26L_{\mathrm{c}}$).

levels of Fig. 9 are kept the same as those in Fig. 4 (top), which means that the sound field shown in the current plot do not contain any visible sign of interference due to the spurious noise of the synthetic turbulence. In the meantime, it is apparent in Fig. 9 that the WLE case displays weaker sound waves (particularly for those with small wavelengths, i.e. high frequencies) compared to the SLE case plotted on the same scale. This result does agree with the early investigation by Lau, Haeri and Kim [15].

Sound power spectra obtained at the observer point A (denoted in Fig. 4) for both the SLE and WLE cases are plotted in Fig. 10 where a theoretical prediction by Amiet et al. [24, 28, 29] and an experimental measurement performed at the University of Southampton are also included for comparison. It should be noted that the experimental result includes a shear-layer correction and has been scaled up by $(r_{\mathrm{exp}}/L_{\mathrm{c}})^2/(r_{\mathrm{sim}}/L_{\mathrm{c}})$ to match the distance to the observer position and to compensate the 3D decaying rate ($p'_{\mathrm{3D}} \propto r$ & $p'_{\mathrm{2D}} \propto \sqrt{r}$).

Figure 10 shows that the overall levels and shapes of the spectra from the three different (theoretical, experimental and numerical) approaches are in good agreement. However, the numerical result exhibits more pronounced dips and humps in the spectral shape than others, which might indicate that the velocity spectra of the present synthetic turbulence are not sufficiently smooth (see Figs. 3 and 7). Although this anomaly can be reduced by em-

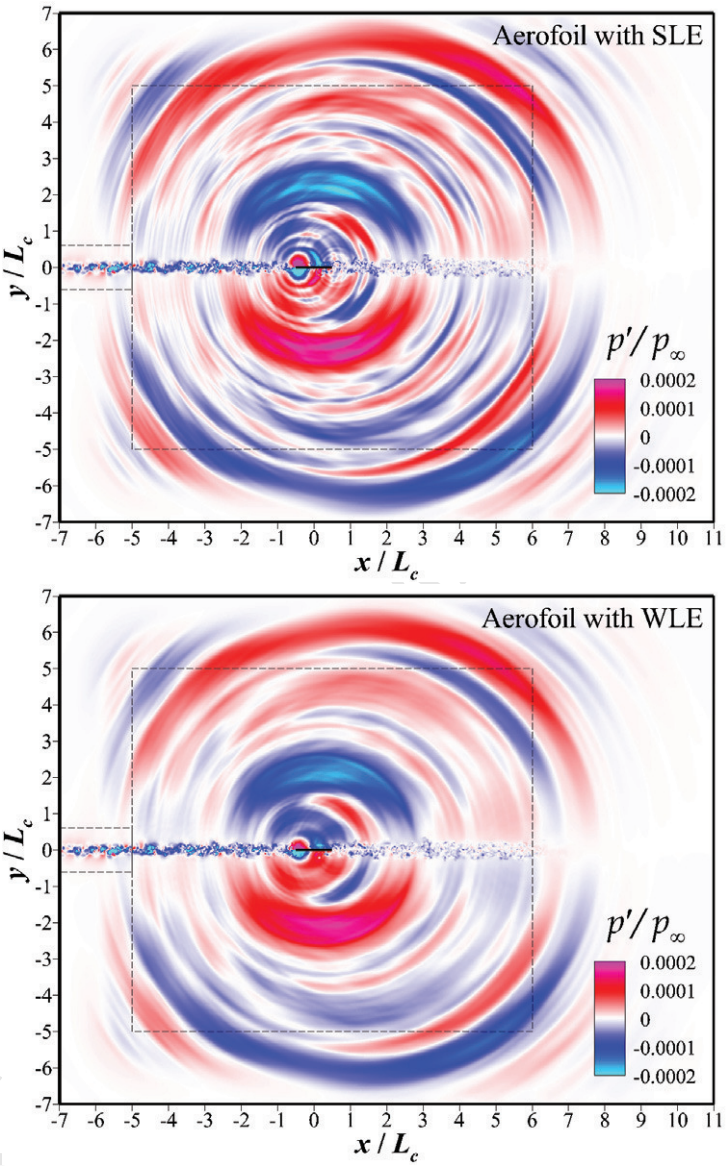

Figure 9: The result of ATI noise simulation obtained at $a_\infty t/L_c = 80$ and taken from an $xy-$plane at the mid-span ($z = 0$). For two different aerofoil geometries: SLE (top) and WLE (bottom). Based on the synthetic turbulence shown in Fig. 7. Same contour levels for both cases up to $\pm 2 \times 10^{-4}$. The location of the aerofoil (of zero thickness) is highlighted with a thick borderline for clarity.

ploying more eddies (and increasing the size of the virtual eddy box) as mentioned at the end of Sec. 3.4, the authors see the current set-up reasonably accurate and efficient for the study of ATI noise and its reduction mechanisms associated with WLE. The effect of WLE is evident in the bottom graph of Fig. 10 where both the simulation and the measurement manifest significant noise reduction (by up to 10dB) particularly in the high-frequency range. It should be noted that the measurement data (particularly in the WLE case) contained a noticeable level of self-noise contributions that seem to have led to a flatter broadband spectrum with a little higher level in the high-frequency range compared to the simulation data. Finally, Fig. 11 is plotted to re-confirm that the spurious noise due to the present synthetic turbulence is sufficiently negligible (20 to 60dB lower than the ATI noise in the entire frequency range resolved).

7. Conclusions

In this paper, an advanced form of SEM (synthetic eddy method) has successfully been developed particularly for 3D aeroacoustic simulations of ATI (aerofoil-turbulence interaction) noise. A total of 15 new constraint parameters to impose an adequate level of control over the randomly distributed eddies were introduced and systematically optimised to create a realistic turbulence statistics based on von Kármán velocity spectra. The full 3D capabilities of the proposed approach with inclusion of spanwise periodic boundary conditions were effectively demonstrated through large-scale numerical simulations. Using the stream of eddies which was narrowed down to target the aerofoil and its vicinity was numerically efficient in three aspects: a) that the amount of computational overhead to create the eddies was minimised; b) that fine meshes to resolve the smallest eddies was not required at the mid and far fields; and c) that an undisturbed clean acoustic environment was preserved in the far field. Under the current computational set-up, it was found that 10 or more number of cells per eddy radius was required to keep the level of spurious noise minimal particularly in the high-frequency range. The new SEM combined with a sponge-layer technique resulted in spurious noise that was 20 to 60dB lower than ATI noise across the entire frequency range. The overall performance of the proposed SEM was successfully demonstrated through the simulation of ATI noise, which was well compared against existing theoretical and experimental data with some moderate discrepancies in the sound spectra. It is envisaged that the

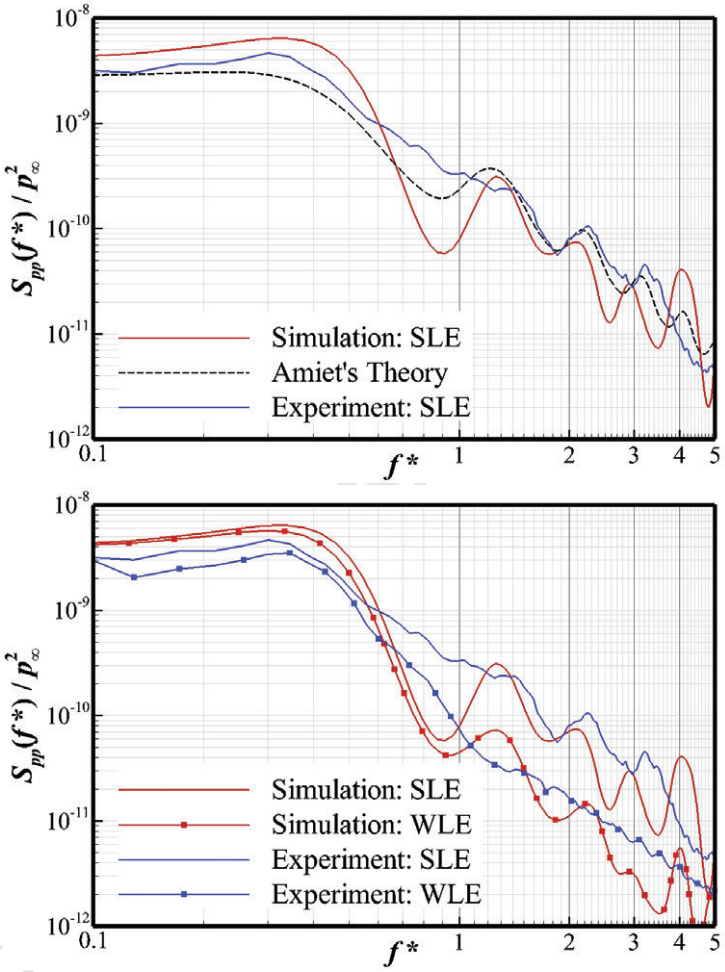

Figure 10: ATI sound spectra obtained at the observer point A shown in Fig. 4. Comparison of the present results with Amiet's theoretical prediction [24, 29] and existing experimental data.

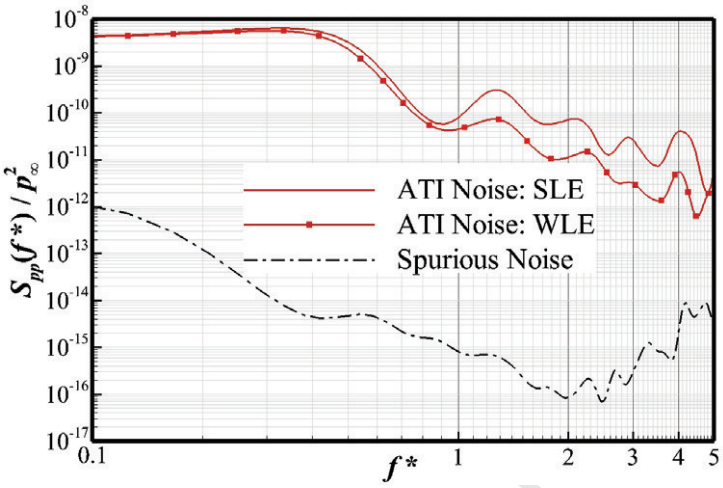

Figure 11: The level of spurious noise generated by the present synthetic turbulence in comparison to those from the physical mechanism of ATI noise.

discrepancies were attributed to the fact that the current velocity spectra were not entirely smooth as those in the counterpart theory and experiment. There is a scope of work in the future to refine the velocity spectra without an excessive increase in the eddy population overburdening the computational cost. In conclusion, the present work offers a solid ground on which numerical simulations can now provide highly reliable data to discover and explain the control mechanisms of ATI noise associated with wavy leading edges.

Acknowledgement

The authors gratefully acknowledge the support of EPSRC (Engineering and Physical Sciences Research Council) for the present work under EP/J007633/1. We give special thanks to Professor Joseph, Dr Subramanian and Mr Paruchuri in ISVR (Institute of Sound and Vibration Research) at the University of Southampton for providing us with their experimental data for comparison. We also acknowledge the high-performance computing facilities and services of the UK National Supercomputer ARCHER and the local IRIDIS-4 at the University of Southampton in the completion of this work.

[1] R. H. Kraichnan, Diffusion by a random velocity field, Physics of Fluids 13 (22) (1970) 22–31.

[2] A. Smirnov, S. Shi, I. Celik, Random flow generation technique for large eddy simulations and particle-dynamics modeling, Journal of Fluids Engineering 123 (2) (2001) 359–371.

[3] P. Batten, U. Goldberg, S. Chakravarthy, Interfacing statistical turbulence closures with large-eddy simulation, AIAA Journal 42 (2004) 485–492.

[4] A. Keating, U. Piomelli, Synthetic generation of inflow velocities for large-eddy simulation, 34th AIAA Fluid Dynamic Conference and Exhibit, Portland, Oregon, aIAA Paper 2004-2547, 2004.

[5] S. H. Huang, Q. S. Li, J. R. Wu, A general inflow turbulence generation for large eddy simulation, Journal of Wind Engineering and Industrial Aerodynamics 98 (10-11) (2010) 600–617.

[6] R. Yu, X. S. Bai, A fully divergence-free method for generation of inhomogeneous and anisotropic turbulence with large spatial variation, Journal of Computatioinal Physics 256 (2014) 234–256.

[7] R. Ewert, Broadband slat noise prediction based on CAA and stochastic sound sources from a fast random particle-mesh (RPM) method, Computers & Fluids 37 (2008) 369–387.

[8] M. Dieste, G. Gabard, Random particle methods applied to braodband fan interfaction noise, Journal of Computational Physics 231 (2012) 369–387.

[9] N. Jarrin, S. Benhamadouche, D. Laurence, R. Prosser, A synthetic-eddy method for generating inflow conditions for large-eddy simulations, International Journal of Heat and Fluid Flow 27 (4) (2006) 585–593.

[10] M. Pamies, P. E. Weiss, E. Garnier, S. Deck, Generation of synthetic turbulent inflow data for large eddy simulation of spatially evolving wall-bounded flows, Physics of Fluids 21 (045103) (2009) 1–15.

[11] R. Poletto, T. Craft, A. Revell, A new divergence free synthetic eddy method for the reproduction of inlet flow conditions for LES, Flow, Turbulence and Combustion 91 (3) (2013) 519–539.

[12] A. Sescu, R. Hixon, Toward low-noise synthetic turbulent inflow conditions for aeroacoustic calculations, International Journal for Numerical Methods in Fluids 73 (12) (2013) 1001–1010.

[13] J. W. Kim, A. S. H. Lau, N. D. Sandham, Proposed boundary conditions for gust-airfoil interaction noise, AIAA Journal 48 (11) (2010) 2705–2710.

[14] J. W. Kim, A. S. H. Lau, N. D. Sandham, CAA boundary conditions for airfoil noise due to high-frequency gusts, Proceedia Engineering 6 (2010) 244–253.

[15] A. S. H. Lau, S. Haeri, J. W. Kim, The effect of wavy leading edges on aerofoil-gust interaction noise, Journal of Sound and Vibration 332 (2013) 6234–6253.

[16] T. S. Lund, X. Wu, K. D. Squires, Generation of turbulent inflow data for spatially-developing boundary layer simulations, Journal of Computational Physics 140 (1998) 223–258.

[17] A. S. Monin, A. M. Yaglom, Statistical fluid mechanics: mechanics of turbulence, vol. 2, MIT Press, 1975.

[18] V. Clair, C. Polacsek, T. L. Garrec, G. Reboul, M. Gruber, P. Joseph, Experimental and numerical investigation of turbulence-airfoil noise reduction using wavy edges, AIAA Journal 51 (11) (2013) 2695–2713.

[19] J. W. Kim, Optimised boundary compact finite difference schemes for computational aeroacoustics, Journal of Computational Physics 225 (2007) 995–1019.

[20] J. W. Kim, High-order compact filters with variable cut-off wavenumbers and stable boundary treatment, Computers & Fluids 39 (2010) 1168–1182.

[21] J. W. Kim, D. J. Lee, Generalized characteristic boundary conditions for computational aeroacoustics, AIAA Journal 38 (11) (2000) 2040–2049.

[22] J. W. Kim, Quasi-disjoint pentadiagonal matrix systems for the parallelization of compact finite-difference schemes and filters, Journal of Computational Physics 241 (2013) 168–194.

[23] P. Chakraborty, S. Balachandar, R. J. Adrian, On the relationships between local vortex identification schemes, Journal of Fluid Mechanics 535 (2005) 189–214.

[24] R. K. Amiet, Acoustic radiation from an airfoil in a turbulent stream, Journal of Sound and Vibration 41 (1975) 407–420.

[25] M. E. Goldstein, Unsteady vortical and entropic distortions of potential flows around arbitrary obstacles, Journal of Fluid Mechanics 89 (1978) 433–468.

[26] J. W. Kim, D. J. Lee, Generalized characteristic boundary conditions for computational aeroacoustics, part 2, AIAA Journal 42 (1) (2004) 47–55.

[27] R. D. Sandberg, N. D. Sandham, Direct numerical simulation of turbulent flow past a trailing edge and the associated noise generation, Journal of Fluid Mechanics 596 (2008) 353–385.

[28] M. Roger, S. Moreau, Extensions and limitations of analytical airfoil broadband noise models, International Journal of Aeroacoustics 9 (3) (2010) 273–305.

[29] V. P. Blandeau, P. F. Joseph, G. Jenkins, C. J. Powles, Comparison of sound power radiation from isolated airfoils and cascades in a turbulent flow, Journal of the Acoustical Society of America 129 (2011) 3521–3530.